Journal of Applied Electrochemistry (2021) 51:567–580
https://doi.org/10.1007/s10800-020-01517-x

RESEARCH ARTICLE

Corrosion properties of ceria-based coating electrodeposited from alkaline bath on electrogalvanized steel

F. Rouabhia[1] · Y. Hamlaoui[1] · A. Meroufel[2] · F. Pedraza[3]

Received: 21 August 2020 / Accepted: 7 December 2020 / Published online: 6 January 2021

Abstract

Long-term protectiveness of zinc coatings remains challenging where conversion surface pre-treatments are suggested such as the promising cerium oxide-based coatings. In the present work, the effect of acetic acid addition and of temperature of the bath on the ceria-based coatings produced by cathodic electrodeposition on electrogalvanized steel are investigated. The electrochemical, surface chemistry, and topographical properties are characterized and their corrosion performance is evaluated in NaCl solution. The results show that the coatings prepared from equimolar mixture of cerium chloride and acetic acid at pH 8 and room temperature were less cracked, had a smaller grain size, and offered a three-fold increase of the corrosion resistance when compared with those prepared in cerium chloride solution at pH 6. From X-ray diffraction patterns, it seems that the deposits obtained at pH 8 are free from corrosion products. Moreover, the porosity of the coatings obtained at pH 8 increases with increasing the bath temperatures indicating that at high bath temperature the deposits become heterogeneous and do not cover the whole surface of the substrate.

Graphic abstract

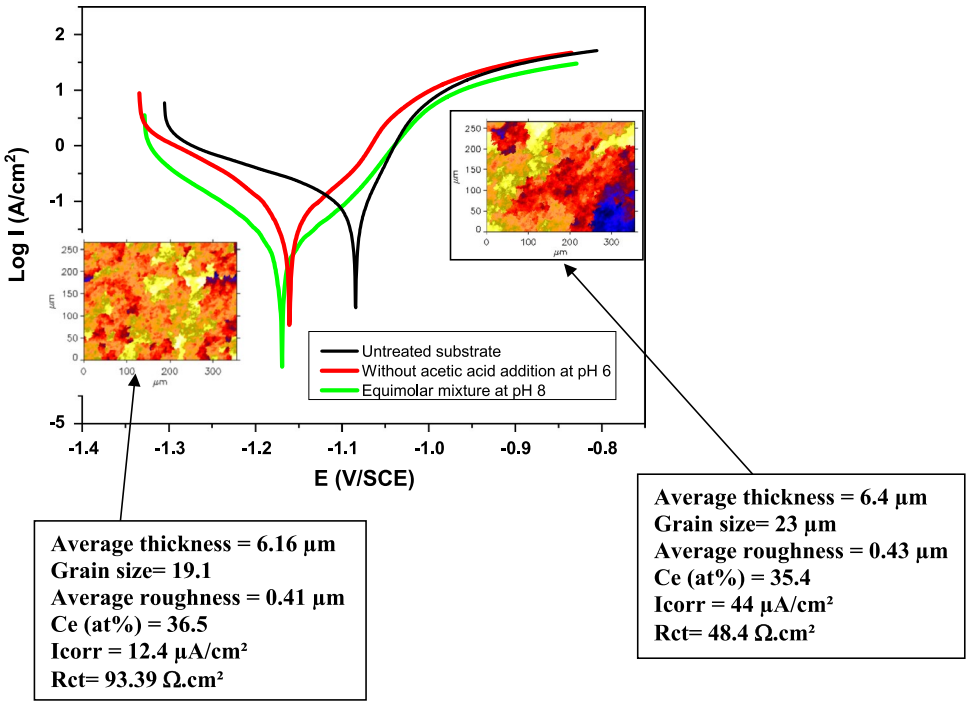

Keywords Electrogalvanized steel · Cerium oxide coating · Acetic acid · Cathodic electrodeposition · Corrosion

Extended author information available on the last page of the article

1 Introduction

Zinc coatings are widely applied on fasteners like bolts for automobiles, marine platforms, concrete structures, and other sectors because of their many advantages including their relatively higher corrosion resistance, accepted aesthetic appearance, and lower cost compared to uncoated steel [1]. Galvanized coatings protect steel by providing first an active sacrificial phase followed by passive phase with excellent barrier properties against the electrolyte penetration that isolates the steel substrate [2]. However, for extended corrosion protection performance, the Zn-based coatings require additional protection including post-plate chromating, which is at stake due to its carcinogenic effect [3, 4]. Alternatively, cerium-based compounds were identified as environmentally safe conversion coatings to replace the carcinogenic Cr(VI). Indeed, cerium-based coatings were successfully used on many substrates including stainless steel [5, 6], magnesium [7], and aluminum alloys [8]. However, the coatings did not show good corrosion performance on low carbon steel and zinc metal in the long term in saline environments [6, 9, 10]. This poor performance was attributed to the acidic character of deposition solution particularly for high concentrations of cerium salt. It was found that the acidic pH of the deposition solution promotes the dissolution of the substrate before or during the coating deposition.

According to the Pourbaix diagram of zinc, the acidic medium induces high corrosion and the formation of unstable products contrary to the neutral or weakly alkaline condition [11]. Some investigations showed that by optimizing the added agents such as H_2O_2 [5], fluoroalkylsilane [12], poly(diallyldimethylammonium chloride) (PDDA) or polyethylenimine (PEI) [13], and the electrodeposition process parameters [6, 14, 15], better corrosion resistance of ceria-based coatings was obtained compared to the chemical deposition method [7]. Also, the addition of organic additives showed interesting improvement of the corrosion resistance by reducing defects and cracks in the conversion coatings [16–23]. However, the organic additives may significantly modify the chemical deposition method. Wang and Golden [24, 25] demonstrated the possibility of ceria-based coatings deposition from alkaline baths by anodic deposition method. The authors showed that the addition of a weak acid (like acetic acid) to the cerium salt bath delayed the precipitation of cerium hydroxide and induced the dissociation of the cerium complex releasing Ce^{3+} ions in the solution. Indeed, the addition of acetic acid maintained a solution pH above 7 without cerium hydroxide precipitation and release of free Ce^{3+} ions necessary for the formation of $Ce(OH)_3$. This can be attributed to the formation of non-bonded cerium acetate complex as suggested in the previous works [22, 25] according to Eq. (1):

$$Ce^{3+} + 3\,CH_3COOH \rightleftarrows Ce(CHCOO)_3 + 3\,H^+. \quad (1)$$

Recently, Bourenane et al. [26] have shown that ceria-based coatings electrodeposited on low carbon steel from cerium nitrate solution in the presence of a low acetic acid concentration at pH 8 were homogeneous and protective against corrosion for longer immersion time in NaCl solution. However, the films obtained at solution pH seemed to be more heterogeneous and contained cracks losing thus quickly its effectiveness with increasing bath temperature [27]. According to the literature [15, 28–30], the electrochemical mechanism of cathodic electrodeposition involves a first step of reduction of water and of dissolved oxygen to produce hydroxide ions from which different cerium oxyhydroxides precipitate. However, raising the bath temperature enhances the hydrogen evolution reaction (HER) by water reduction and fosters substrate dissolution [31–33]. This phenomenon would make the voltammetry tests at bath temperatures above 55 °C quite difficult and increase the diffusion coefficient of dissolved oxygen. However, according to Henry's law, the increase in the bath temperature decreases the concentration of dissolved oxygen, which in turn lowers the deposited amount of $Ce(OH)_3$ and little is known on the mechanisms of formation of the deposits [27].

In light of the above, the mechanism of formation of cathodically electrodeposited ceria-based coatings from alkaline bath is investigated in this work using analytical and electrochemical methods. It is noted that $CeCl_3$ was chosen instead of $Ce(NO_3)_3$ since it provides more adherent and uniform coatings [28] but precaution was taken to prevent pitting corrosion due to the presence of chloride ions namely at elevated bath temperature. Therefore, the effect of the acetic acid concentration and bath temperature on the corrosion protection of the coatings is investigated.

2 Experimental

2.1 Materials

14 mm round samples of A366 cold-rolled carbon steel (Fe–0.13C–0.041Mn–0.04S–0.012N–0.55Cu, wt%-nominal composition) were electroplated with zinc from a stirred bath (50 g L^{-1} $ZnCl_2$, 240 g L^{-1} KCl, and 63 g L^{-1} H_3BO_3 at pH 4.5) at 40 °C by applying 70 mA cm^{-2} for 20 min. Further details on the electrodeposition procedure can be found in previous works [34, 35]. Before each experiment, the electrode surface is pickled in 0.6% HNO_3 for 10 s to remove any surface impurity or corrosion product, cleaned ultrasonically for 3 min with ethanol, and then rinsed with water and immediately dried with hot pulsed air.

2.2 Cathodic electrodeposition and electrochemical tests

A 10^{-2} M aqueous solution of $CeCl_3{\cdot}7H_2O$ (Aldrich, ≥ 99% pure) was used as electrodeposition bath. Different concentrations (between 10^{-3} and 2 M) of acetic acid were added as complexing agent. The pH of the solution was adjusted by adding drops of 1 M NaOH every 5 min. The cerium conversion coatings were deposited by cathodic deposition during 20 min applying a current density of 1.5 mA cm^{-2} using a three-electrode configuration set-up. The three electrodes were the electrogalvanized carbon steel substrate as the cathode, platinum grid as counter electrode, and a saturated calomel electrode (SCE) as the reference one. Dissolved oxygen at different bath temperature was measured by using a multi-parameters probe HI 9828 of Hana instruments. The electrochemical tests were carried out using a potentiostat/galvanostat (EC-Lab P150, Biologic).

The same experimental set-up was used for the corrosion tests in 0.5 M NaCl under stirring. Cyclic voltammetry was recorded from − 1.0 to − 2.0 V/SCE at 1 mV s^{-1} of scanning rate. All the corrosion tests were repeated at least three times for reproducibility. They were carried out at room temperature, except for the study on the effect of the bath temperature for which the temperatures ranged between 25 and 55 °C. Prior to any electrochemical test, the time to stabilization of the open circuit potential was 30 min. The Tafel polarization curves were obtained at a scanning rate of 0.5 mV s^{-1} around ± 250 mV with respect the open circuit potential (E_{ocp}). The polarization resistance (R_p) was measured at 0.5 mV s^{-1} of scan rate, and the derived values were obtained at 20 mV away (cathodic and anodic domains) of the corrosion potential (E_{corr}). The impedance data were recorded at the corrosion potential (E_{corr}) between 500 kHz and 100 MHz at 10 mV as the applied sinusoidal perturbation. The EIS results were fitted using Zview program.

2.3 Characterization of the films

The surface topography was characterized by non-contact white-light optical profilometry using a white light interferometer (WLI FL from FRT). Imaging of the surface of the samples was conducted using vertical scanning interferometry (VSI) mode with full resolution. The analysis of the surface roughness, thickness, and grain size was performed using FRT Mark III® software. The surfaces were also observed with a Zeiss Axio Imager M1 Trinocular Frame optical microscope. Moreover, the surface morphology was analyzed more thoroughly using a scanning electron microscope (SEM) of FEI Quanta 250 equipped with X-ray energy-dispersive spectroscopy (EDS) for chemical analysis. The crystalline phases present in the deposits were investigated by X-ray diffraction (XRD) in the θ–2θ configuration using CuK_α radiation $\lambda = 1.5406$ nm (Bruker AXS D8-Advanced diffractometer).

3 Results and discussion

3.1 Effect of the acetic acid addition

Figure 1 shows the evolution of the substrate potential during deposition in 10^{-2} M $CeCl_3$ for different acetic acid concentrations at room temperature. The solution pH with acetic acid was adjusted to 8, whereas without acetic acid was only adjusted to 6 to avoid precipitation of cerium hydroxide [26]. The curves show that the substrate potential shifts towards more negative values before stabilization, which indicates full surface coverage by the ceria-based coating. Moreover, the fastest shift of potential towards more negative values occurs for the deposits grown from the equimolar mixture (10^{-2} M $CeCl_3$ and 10^{-2} M acetic acid at pH 8). Since the curves display the same shape, it can be assumed that the mechanism of formation is similar but that the deposits grow thicker under these conditions.

However, by increasing the acid concentration above 10^{-2} M, the potential shifts towards less negative (cathodic) values (near the substrate potential), which suggests that the deposition process is limited by the amount of free Ce^{3+} species in the solution. According to the literature [26, 36] and to the current experimental data, the amount of Ce^{3+} decreases with the increase of acetic acid concentration. From 1 M acetic acid, no Ce^{3+} is available in the solution (Table 1).

A linear relationship with a slope of 0.7 was observed between the steady state potential of the substrate and the

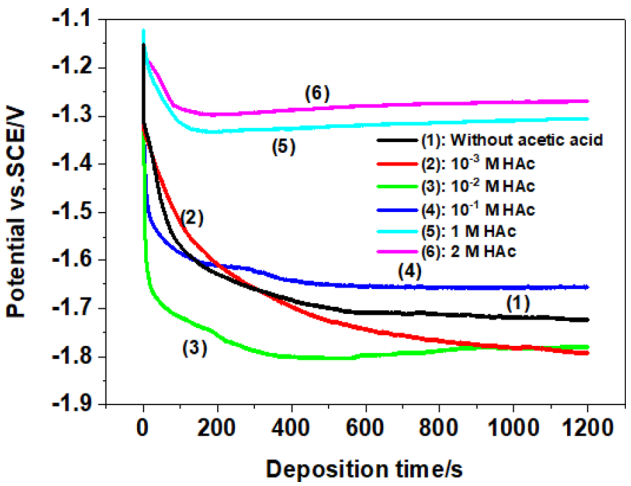

Fig. 1 Evolution of substrate potential with deposition time in 10^{-2} M $CeCl_3$ without (at pH 6) and with different acetic acid (HAc) concentrations (at pH 8) performed at − 1.5 mA cm^{-2} and room temperature

Table 1 Electrochemical parameters, free cerium species, and acetate cerium complex calculated from the cerium chloride solution with different acetic acid concentrations

[CH_3COOH] (M)	00	10^{-3}	10^{-2}	0.1	1	2
ΔpH	1.546	0.613	0.260	0	0	0
Final potential vs. SCE/V	− 1.72	− 1.79	− 1.78	− 1.65	− 1.31	− 1.27
[$Ce(CH_3COO)_3$] (M)	0	3.14×10^{-4}	2.918×10^{-3}	9.99×10^{-3}	10^{-2}	10^{-2}
Free [Ce^{3+}] (M)	10^{-2}	9.68×10^{-3}	7.082×10^{-3}	5.99×10^{-5}	0	0
E reversal vs. SCE/V	–	–	–	− 1.86	− 1.81	− 1.54
E wave vs. SCE/V	− 1.34	− 1.30	− 1.26	− 1.21	− 1.16	− 1.16

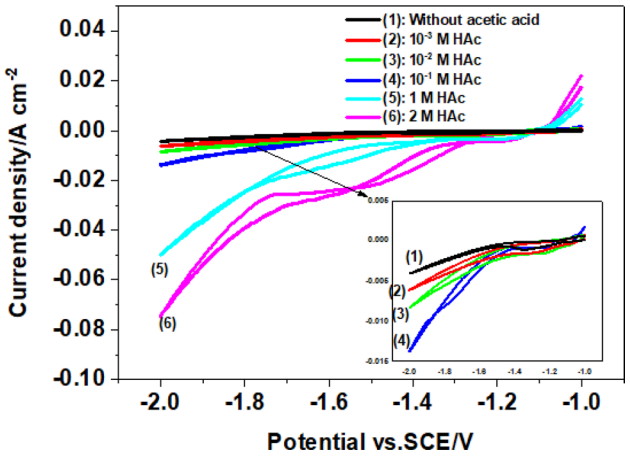

Fig. 2 Cyclic voltammograms performed at 20 mV s^{-1} in 10^{-2} M $CeCl_3$ without (at pH 6) and with different acetic acid (HAc) concentrations (at pH 8) and room temperature

solution pH. This result indicates the transfer of one electron that confirms that acetic acid does not influence the mechanism of the electrodeposition. To confirm the non-influence of acetic acid addition on the mechanism, cyclic polarization curves were recorded in the $CeCl_3$ solution with different concentrations of acetic acid (Fig. 2). It can be clearly observed that the voltammograms recorded in the solution without acetic acid and with less than 10^{-2} M present a uniform hysteresis that becomes more significant with increasing acetic acid concentration. However, above 10^{-2} M of acetic acid, reversal points between the forward and the reverse scan are observed at − 1.86, − 1.81, and − 1.54 vs. SCE/V for 0.1, 1, and 2 M acetic acid, respectively (see Table 2). This electrochemical behavior is characterized by a low current density compared to the one observed during the forward scan and can be attributed to the decomposition of the cerium acetate complex. This hypothesis is supported by the absence of this phenomenon on the voltammograms obtained from cerium chloride solution with and without low cerium acetate concentration (see Table 2). In addition, no reverse scan is recorded in the cyclic polarization curve (Fig. 3) in the sodium acetate solution at room temperature and pH 8. The cyclic polarization curves obtained with and without acetic acid concentration lower than 10^{-2} M also show an electrochemical wave well defined at low concentration that tends to disappear with increasing the acid concentration (Fig. 2, Table 2). This wave was reported to result from the reduction of oxygen or of Ce(IV) species [15].

Based on the UV results(Fig. 4), the increase of acetic acid concentration brought about the disappearance of the absorption peak at ~ 300 nm that corresponds to the Ce^{4+} ions [5, 37] and the appearance of a new absorption peak appeared at 205 nm attributed to the of acetic acid [38]. Therefore, no free Ce^{3+} species seems to be available in the solution. In addition, while the peaks of Ce^{4+} at 211 and 221 nm [5, 39] remain unchanged, the ones located at 247 and 260 nm shifted slightly towards higher wavelength, which suggests complexation in the form of cerium acetate.

The influence of acetic acid on the surface morphology of the coating surface is displayed in Fig. 5. It can be observed that the electrodeposits obtained from the equimolar mixture appear compact, are less cracked and cover the whole of the exposed surface compared to other concentrations. Conversely, the coating coverage seems weak at high acid concentrations, which agrees with the shift of the electrochemical potential towards the values of the substrate (Fig. 1). The surface morphology of the coatings was also examined by SEM (Fig. 6). No significant difference was observed between the deposits obtained from a solution containing

Table 2 Electrochemical parameters obtained from voltammograms recorded in $CeCl_3$ solution with different acetic acid concentrations at room temperature and pH 8

[CH3COOH] (M)	0	10^{-3}	10^{-2}	0.1	1	2
pH	6	8				
E reversal vs. SCE/V	–	–	–	− 1.86	− 1.81	− 1.54
E wave vs. SCE/V	− 1.34	− 1.30	− 1.26	− 1.21	− 1.16	− 1.16

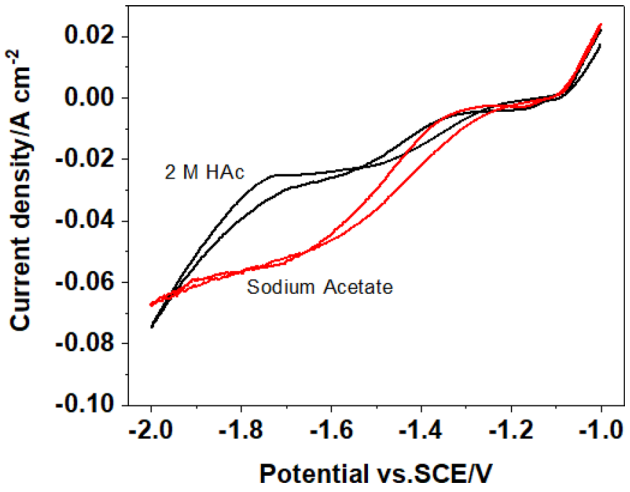

Fig. 3 Cyclic voltammograms of the substrate performed at 20 mV s^{-1} in a mixture of 10^{-2} M $CeCl_3$ + 2 M acetic acid (HAc) and in 2 M sodium acetate solution at pH 8 and room temperature

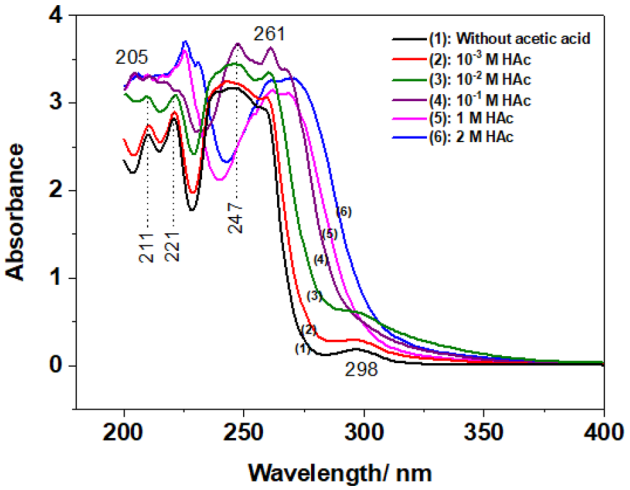

Fig. 4 UV–Vis absorption spectra of 10^{-2} M $CeCl_3$ without (at pH 6) and with different acetic acid concentrations at pH 8

only $CeCl_3$ and the equimolar mixture of cerium salt and acetic acid. In addition, some clusters of cerium oxide particles appear on the top of the coating [15, 21, 40, 41].

The coating parameters such as thickness, grain size, average roughness, and the volume of matter are summarized in Table 3 based on the surface examination by the white light interferometer (WLI). The results show a significant drop in the abovementioned coating properties with the increase of acid concentration above 10^{-2} M, which is consistent with the electrochemical and solution analysis results. Indeed, the Ce amount (at.%) decreases steadily with the increase of the acetic acid concentration and is in line with the decrease of average coating thickness and roughness revealed by optical profilometry. This may be due to the partial dissolution of the substrate during the formation and the growth of the coating as shown in a previous work in cerium nitrate baths [26]. The decrease of grain size with increasing acid concentration can be related to the smoothening effect of acetic acid [20, 42].

3.2 Effect of bath temperature

Figure 7 shows the deposition curves obtained from equimolar mixture at pH 8 and at bath temperatures between 25 and 55 °C. It can be observed that the substrate potential values reached in the deposition solution at 25 °C show a faster drop in potential and subsequent stabilization that indicate a better deposition of cerium hydroxide. However, the increase of the bath temperature above 25 °C seems to considerably slow down the electrodeposition process by reducing the amount of dissolved oxygen in solution (Table 4). This in turn affects the generation of hydroxyl ions (Eqs. (2) and (3)) and the subsequent precipitation of cerium hydroxide species (Eq. (4)).

$$O_2 + 2\,H_2O + 4\,e^- \rightarrow 4OH^- \quad (2)$$

$$O_2 + 2\,H_2O + 2\,e^- \rightarrow 2OH^- + H_2O_2 \quad (3)$$

$$4\,Ce^{3+} + O_2 + 4OH^- + 2\,H_2O \rightarrow 4\,Ce(OH)_2^{2+} \quad (4)$$

The polarization curves shown in Fig. 8 at different temperatures show that the increase of temperature changes the shape of the curves, lowers the hysteresis, and increases their slope towards the cathodic potentials (predominance of the HER) indicating that the surface coverage is less significant at high temperatures as opposed to the single and continuous variation of the potential versus time that characterizes an even deposit [43].

These electrochemical results were confirmed under the SEM micrographs (Fig. 9). The coverage of the deposits prepared from the equimolar solution at pH 8 and − 1.5 mA cm^{-2} for 20 min clearly decreased with the increase of bath temperature, which is accompanied with a decrease of the Ce content in the deposits (Table 5). Moreover, increasing the bath temperature induced a morphology change of the coating from needle-like to a rosette-shaped structure. This may be due to a strong oxidation of Ce^{3+} to Ce^{4+} species and to the degree of coating dehydration causing the destruction of the H-bonds [21, 44–47]. Nevertheless, there appear to be sheet areas rich in zinc and which confirm that the electrogalvanized steel is partially dissolved. Therefore, the porosity rate was calculated from the results of the potentiodynamic polarization using Eq. (5) [48–50]:

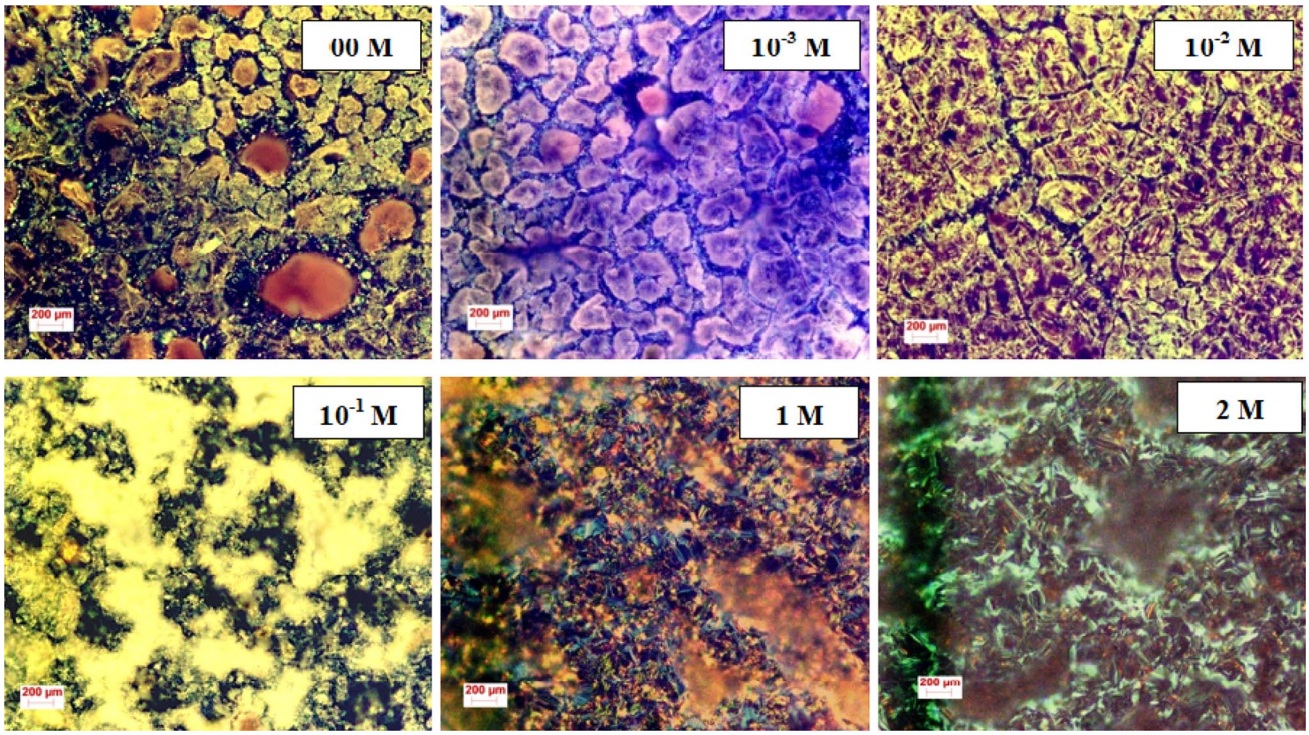

Fig. 5 Optical images (×200) of the deposits obtained at − 1.5 mA cm^{-2} for 20 min in 10^{-2} M $CeCl_3$ without (pH 6) and with different acetic acid concentrations at pH 8

$$\% P = \left(\frac{R_{ps}}{R_p}\right) \times 10^{-\left(\Delta E_{corr}/\beta_a\right)} \times 100, \quad (5)$$

where R_{ps} and R_p are, respectively, the polarization resistances of the untreated and chemically treated samples; ΔE_{corr} is the difference between the corrosion potentials of the untreated and chemically treated samples. β_a is referred to the slope of the anodic Tafel line derived from the polarization curves. R_{ps} and β_a derived from the polarization curves for untreated samples are 66 Ω cm^{-2} and 46 mV/dec, respectively.

The calculated porosity values of the coatings grown at different bath temperatures to be exposed to corrosion in 0.5 M NaCl are shown in Table 6. The temperature increases up to 45 °C induced a decrease in the polarization resistance and an increase in the porosity of the coatings. This result can be discussed on the basis of an increase in cracks which are mainly associated with the formation of gas bubbles (hydrogen evolution reaction) during the electrodeposition process. However, for the coating obtained at 55 °C, the higher porosity value (54%) would suggest a very low surface coverage. This may be due either to the important reduction in the electrodeposited cerium hydroxide amount (see Fig. 7) and to the hydrogen evolution reaction indicated by the high cathodic current density value reached at − 2 vs. SCE/V (Fig. 8).

To confirm this behavior, the surface morphology of the samples was examined by a white light interferometer (WLI) measurements and the results are presented in 2D images as shown in Fig. 10 and the calculated parameters of the film are gathered in Table 7. The WLI images clearly show that the average thickness of the film decreases with increasing bath temperature. It is also noticed that the darker the color of the area or spots in the 2D images, the thinner the deposit, i.e., the black areas are thus attributed to the surface of the substrate. The increase in average roughness values calculated with the FRT Mark III software (Table 7) can be attributed to the formation of a thin or a heterogeneous film on the surface of the substrate [51]. Moreover, it seems that the increase of the bath temperature increases the grain size of the obtained deposits which may be due to the formation at high bath temperature of a deposit rich in cerium oxide contrary to the deposits obtained at low bath temperature which is rich in cerium hydroxide [27, 50].

3.3 Comparative study of the electrochemical properties

To assess the coating corrosion protection performance, the electrochemical behavior of the coatings obtained from linear polarization, Tafel plots, and electrochemical impedance spectroscopy in the equimolar mixture at pH 8 (formed at

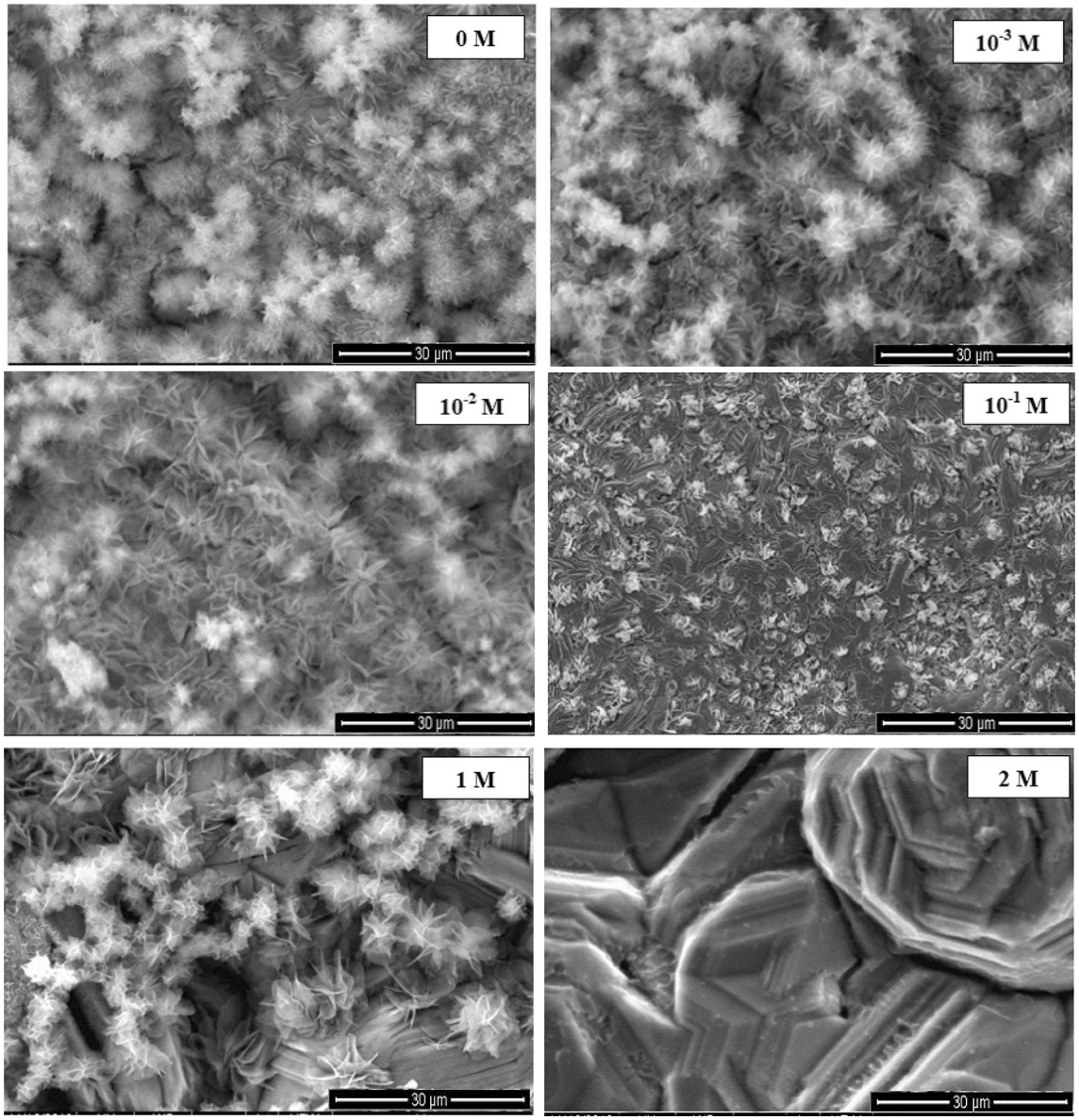

Fig. 6 SEM images of the deposits obtained at − 1.5 mA cm^{-2} for 20 min in 10^{-2} M $CeCl_3$ without (pH 6) and with different acetic acid concentrations at pH 8

Table 3 Content of Ce (at.%) (EDS analysis) and surface parameters calculated by using FRT MARK III of the ceria-based coatings prepared at − 1.5 mA cm^{-2} from 10^{-2} M $CeCl_3$ with different concentrations of acetic acid at pH 8 and at room temperature

[CH_3COOH] (M)	[Ce] (at.%)	Thickness (µm)	Grain size (nm)	Roughness (µm)
Without	35.4	6.4	23	0.43
10^{-3}	35.9	6.3	21	0.42
10^{-2}	36.5	6.2	19	0.41
10^{-1}	16.2	5.4	20	0.34
1	13.9	5.2	12	0.25
2	10	5.1	11	0.24

25 °C), from bath without acetic acid addition at pH 6, and the untreated substrate as reference was evaluated in 0.5 M NaCl solution.

Figure 11 shows the polarization curves of the untreated and treated samples and the calculated parameters, i.e., corrosion potential (E_{corr}), polarization resistance (R_p), anodic and cathodic Tafel slopes (β_a and β_c) and corrosion current density (I_{corr}) are gathered in Table 8. It was observed that both the anodic slope increased slightly while the cathodic slope decreases markedly with the treatments (acetic acid and equimolar mixture). However, the displacement of the corrosion potential towards cathodic values suggests a mixed-type inhibition mechanism. From the corrosion

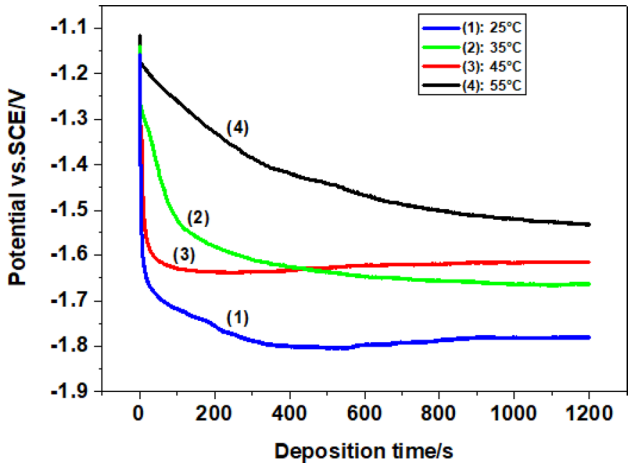

Fig. 7 Evolution of the potential with time of the substrate performed at − 1.5 mA cm^{-2} in equimolar mixture at pH 8 and at different bath temperatures

Table 4 Soluble oxygen concentration in the deposition solution measured at different bath temperatures

Bath temperature (°C)	15	25	35	45	55
O_2 solubility (mg L^{-1})	10.06	8.26	6.91	5.94	5.10

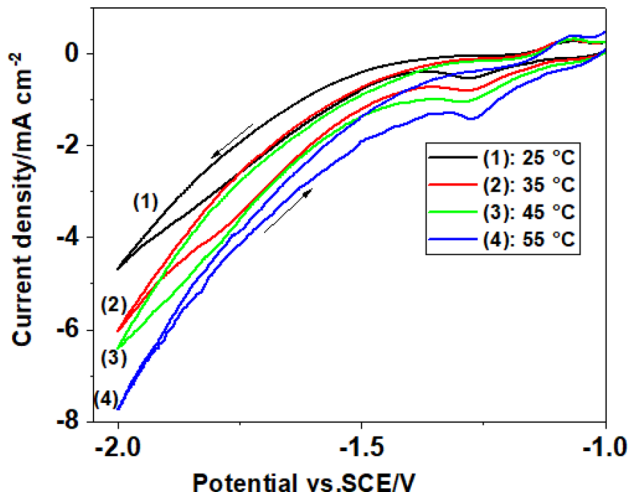

Fig. 8 Cyclic voltammograms performed at 20 mV s^{-1} for the substrate in equimolar mixture at pH 8 and room temperature

current densities, it is also noted that both coatings inhibit the corrosion process but the equimolar mixture is more effective where the I_{corr} is decreased by 3 and 9 times compared to the coating prepared without acetic acid and the untreated substrate, respectively. As expected, the decrease of the I_{corr} and conversely, the increase of the polarization resistance let us to conclude that both coatings act as physical barrier for the mass and charge transfer providing a high degree of corrosion resistance.

To obtain further mechanistic information, EIS measurements were carried out in 0.5 M NaCl solution at room temperature in the frequency range between 10^5 and 0.1 Hz. The samples were set in the test solution for 30 min to attain steady state of the potential. Both Nyquist and Bode diagrams are presented in Fig. 12 for equimolar ceria coated and non-coated (electrogalvanized steel). A first depressed semi-circle followed by a second one non-completely defined are observed in Nyquist diagram (Fig. 12a). Such result would suggest two time constants that can be confirmed through the presence of two peaks in Bode phase angle diagram (Fig. 12b). However, the second time constant is not well defined in the case of equimolar ceria coating which may need to extend the frequency range scan to 10^{-3} Hz. The comparison of uncoated and coated samples shows a slight increase of phase angle of the first time constant and its shifting toward high frequencies for the equimolar ceria coating. Similar findings were obtained by Ferreira et al. [52] when applying ceria and silane pre-treatment on hot-dip galvanized steel. This observation associated with the increase of low-frequency impedance supports a protective process reducing the corrosion rate which is in line with potentiodynamic findings.

The EIS plots (Fig. 12) were analyzed using the Zview software with a proposed equivalent electrical circuit shown in the same figure. The equivalent circuit consists of two time constants with R_c and R_{ct} representing the coating and charge transfer resistances, respectively. CPE_{dl} and CPE_c (constant phase element) are the non-ideal double layer and the coating capacitance, respectively. As supported by the findings of surface characterization, the inhomogeneity of the surface is fixed during EIS fitting by the use of CPE and non-linearity coefficient ($0 < n < 1$). The use of the CPE is dictated when a dispersion of the capacitive loop (depressed semi-circle) is observed. For galvanized steel in NaCl solution, several authors [35, 52–54] obtained two time constants. The first one appeared at intermediate frequencies followed by another at low frequencies (LF). The latter was

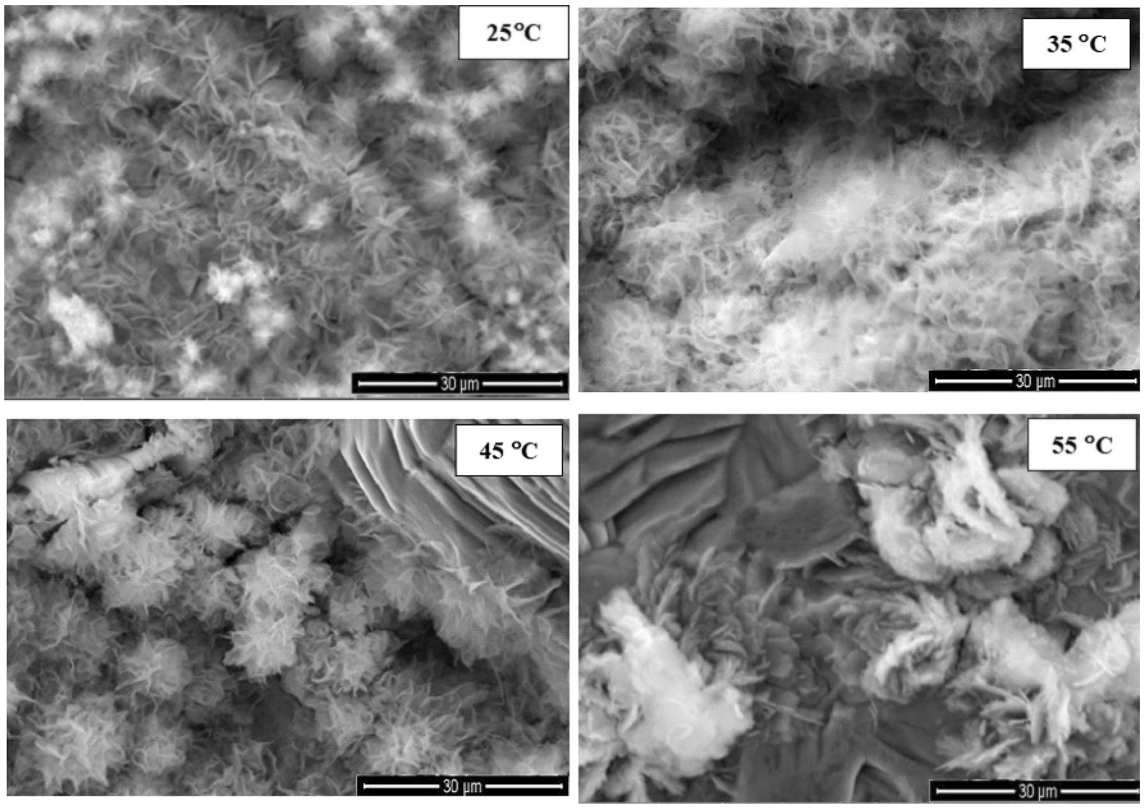

Fig. 9 SEM images for the deposits obtained at − 1.5 mA cm^{-2} from equimolar mixture at pH 8 and at different bath temperatures

Table 5 EDS analysis of the surface of the deposits obtained at − 1.5 mA cm^{-2} during 20 min and at different bath temperatures

	Bath temperature (°C)				
	15	25	35	45	55
Ce (at.%)	13.3	18.7	8.2	6.2	5.7

Table 6 Electrochemical parameters and porosity values of the coatings obtained at different bath temperatures

Bath temperature (°C)	R_p (Ω cm^{-2})	ΔE_{corr} vs. SCE/mV	$P \pm 0.5$ (%)
25	130	75	1
35	86	57	4
45	71	51	7
55	67	12	54

related to the oxide layer formed, as also observed in the present study. However, for the cerium oxy-hydroxide electrodeposits, two contributions can be observed: (i) one in the higher frequency range corresponding to the response of the conversion layer response and (ii) another one in the low frequency range associated with the corrosion process of the whole material as discussed in the previous works [55, 56].

Table 9 shows the increase of R_{ct} values for the coated samples confirming an increase of the corrosion resistance of the substrate. Moreover, the decrease of the double-layer capacitance may result from the relatively lower constant dielectric of the coating due to water uptake [10, 57]. It is also noted that the coating resistance is higher when formed in equimolar mixture at pH 8 up to 4 times than the uncoated galvanized steel.

Based on the electrochemical results and surface morphology observation, the beneficial behavior of the coating obtained from the equimolar mixture at pH 8 compared to that obtained at pH of 6 is mainly attributed to the decrease

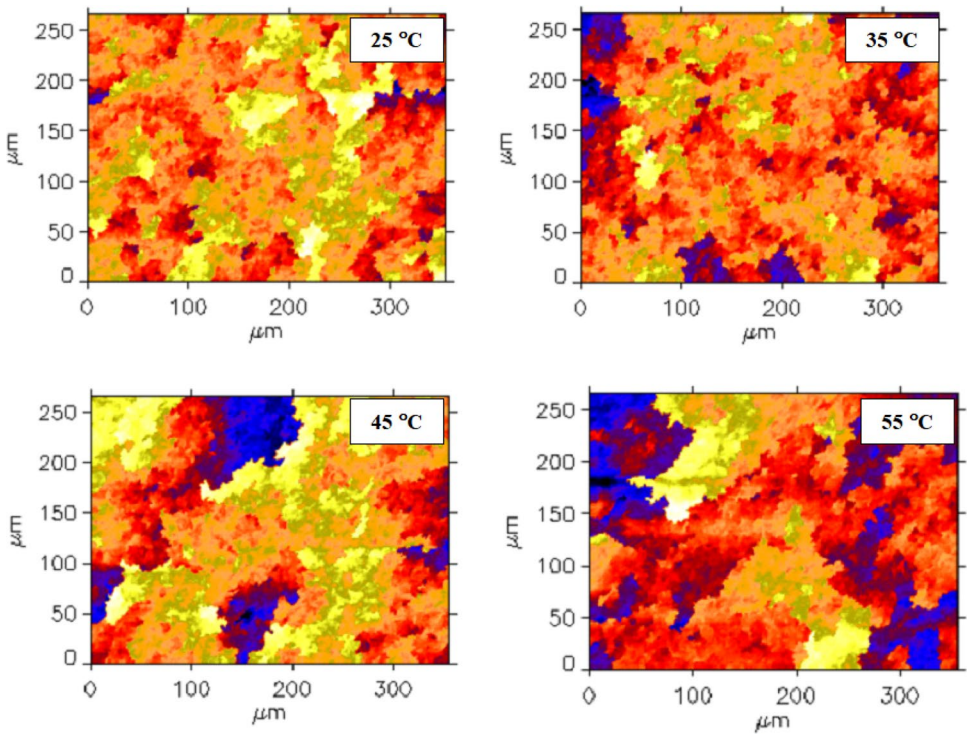

Fig. 10 WLI (white light interferometer, two dimensions) images of the surface morphologies for the coatings obtained at − 1.5 mA cm^{-2} from equimolar mixture at pH 8 and at different bath temperatures

Table 7 Surface parameters of ceria-based coating obtained on electrogalvanized steel from 0.01 M $CeCl_3$ and 0.01 M acetic acid at pH 8 and at different bath temperatures

Bath temperature (°C)	Average thickness (µm)	Grain size (nm)	Roughness (µm)
25	6.16	19.1	0.41
35	6.1	23	0.43
45	5.75	18.02	0.479
55	5.37	37	0.52

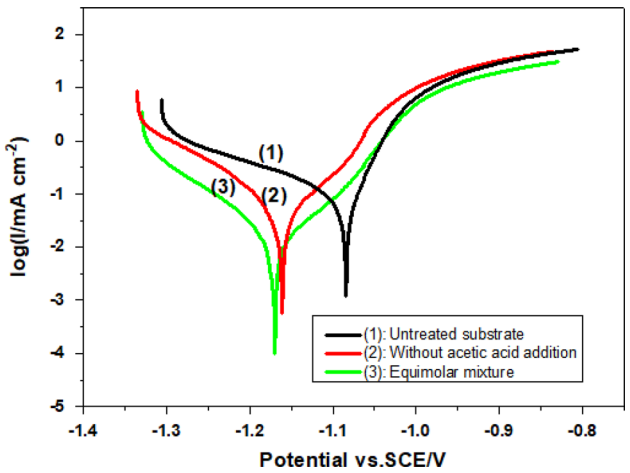

Fig. 11 Potentiodynamic polarization curves for the untreated and coated substrate in 0.5 M NaCl solution and room temperature

of the porosity and cracks of the deposits and the absence of corrosion products. Both the coating defects and the corrosion products are believed to be induced particularly by the hydrogen evolution during electrodeposition process. Indeed, it has been shown in previous work [35] that for lower pH solution or outside the zinc immunity area (defined in Pourbaix Diagram), the substrate dissolution can occur just after immersion of the electrode in the electrodeposition bath leading to the formation of corrosion products under the formed coating, which can strongly alter the adherence and the stability of the obtained electrodeposits. To this end, XRD patterns were performed to identify the crystallographic structure for both coatings (Fig. 13). The results of the various analyses performed on the CeO_2 precipitate obtained from equimolar mixture and NaOH are presented in Fig. 13a. The XRD pattern is typical of ceria (CeO_2) (JCPDS 004–0593) as reported in literature [58]. The pattern of the coating obtained from $CeCl_3$ solution at pH 6 (Fig. 13b) shows clearly the peaks of CeO_2 and Zn (JCPDS 004-0831). However, the crystal planes (004) and (028) that diffracted at about 10.5 and 41°, respectively, are attributed to $Zn(OH)_2$ $0.5H_2O$ according to the JCPDS 020-1436 card.

In $CeCl_3$ solution at pH 6, the substrate could be exposed to partial dissolution leading to the generation of Zn^{2+} where just after polarization the released species may react with the OH^- species generated at the interface to form zinc hydroxide according to reactions (6) and (7):

Table 8 Polarization parameters of untreated and coated substrate in 0.5 M NaCl solution

Substrate	E_{corr} vs. SCE/mV	R_p (Ω cm^{-2})	β_a (mV)	β_c (mV)	I_{corr} (µA cm^{-2})
Untreated substrate	− 1085.69	162	46.0	193.4	110.25
Without acetic acid addition (pH 6)	− 1147.06	357	62.9	103.9	43.93
Equimolar mixture (pH 8)	− 1170.00	1300	72.4	89.8	12.40

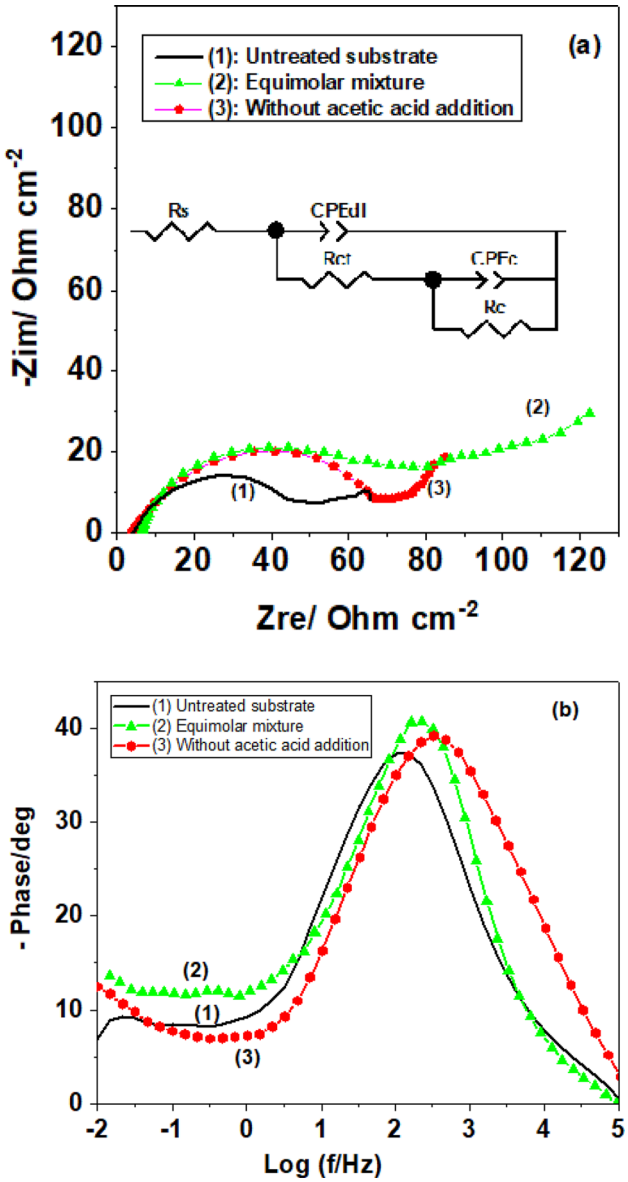

Fig. 12 Electrochemical impedance spectroscopy diagrams for the untreated and coated substrate in 0.5 M NaCl solution and room temperature

$$Zn \rightarrow Zn^{2+} + 2e^{-} \quad (6)$$

$$Zn^{2+} + 2OH^{-} \rightarrow Zn(OH)_2 \quad (7)$$

It can be remarked that this corrosion product was not observed on the pattern of the coating obtained from equimolar mixture at pH 8, which indicates that the coatings are free from corrosion products and are then more stable and more protective against corrosion.

4 Conclusions

Ceria-based coatings were obtained on electrogalvanized steel by cathodic electrodeposition from cerium chloride at basic pH solution where acetic acid was added to form an unbounded complex and to prevent cerium hydroxide precipitation in the solution. The electrochemical results have shown that high acetic acid concentrations seem detrimental to the coating formation. However, an equimolecular (acetic acid/cerium chloride) mixture at pH 8 results in smooth coatings and with a smaller grain size than to the ones obtained at pH 6. Moreover, the increase of the temperature from 25 to 55 °C resulted in lower cerium contents in the deposits but with a change of coating morphology from needle-like to a rosette-shaped structure and a marked decrease of the porosity. The coating surface parameters estimated by white light interferometry show that by increasing the bath temperature, the average thickness of the coating decreases while the surface roughness and the grain size increases. All these results were supported by the XRD spectra showing the absence of corrosion products on the coating obtained at pH 8, which allows us to conclude the superior quality of this coating compared to those obtained at pH 6. This was confirmed through d.c polarization and EIS measurements on both coatings in NaCl solution. High corrosion protection was thus obtained for the coating prepared from equimolar mixture at pH 8 and at room temperature.

Table 9 Fitting results of EIS data for untreated and coated substrate in 0.5 M NaCl solution

Substrate	Electrochemical parameters							
	R_s (Ω cm^2)	CPE_{dl} (mF s$^{(n-1)}$ cm^{-2})	n_{dl}	R_{ct} (Ω cm^2)	CPEc (mF s^{n-1} cm^{-2})	n_c	R_c (Ω cm^2)	χ^2
Untreated	4.17	0.78	0.69	44.19	0.087	0.47	54	2×10^{-3}
Without acetic acid addition	4.14	0.41	0.64	68.42	0.17	0.60	168	8×10^{-3}
Equimolar mixture	4.08	0.38	0.74	93.39	0.048	0.40	235	8×10^{-3}

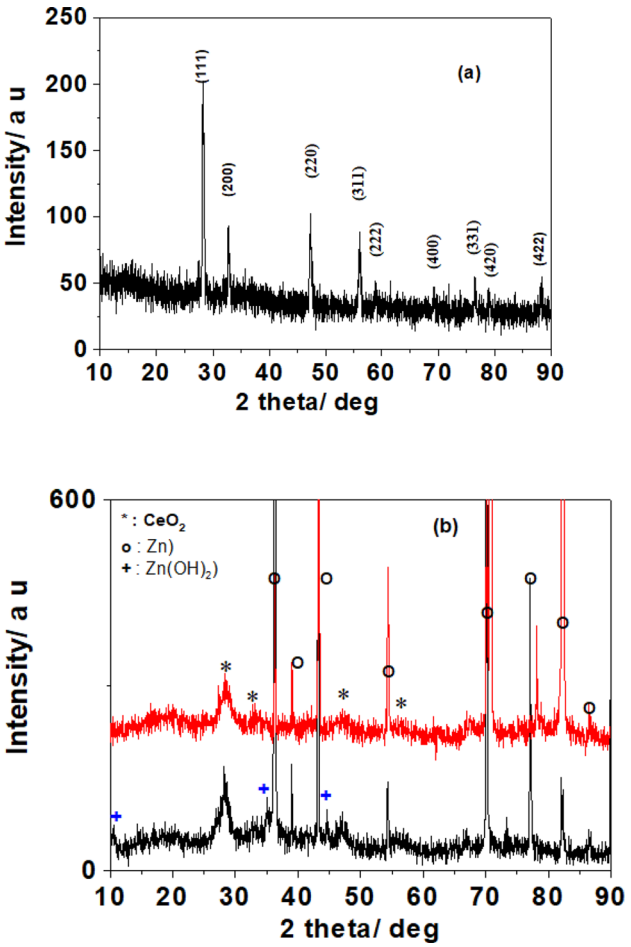

Fig. 13 XRD patterns of **a** the precipitate obtained with alkalinization of equimolar mixture and **b** the ceria-based coatings prepared at − 1.5 mA cm^{-2} and room temperature from equimolar mixture at pH 8 (top) and from 10^{-2} M $CeCl_3$ at pH 6 (bottom)

References

1. Chen YY, Chung SC, Shih HC (2006) Studies on the initial stages of zinc atmospheric corrosion in the presence of chloride. Corros Sci 48:3547–3564. https://doi.org/10.1016/j.corsci.2005.12.007
2. Koç E, Kannan MB, Ünal M, Candan E (2015) Influence of zinc on the microstructure, mechanical properties and in vitro corrosion behavior of magnesium-zinc binary alloys. J Alloy Compd 648(2015):291–296. https://doi.org/10.1016/j.jallcom.2015.06.227
3. Shchukin DG, Zheludkevich M, Yazakau K, Lamaka S, Ferreira MGS, Mohwald H (2006) layer by layer assembled nanocontainers for self healing corrosion protection. Adv Mater 18:1672–1678. https://doi.org/10.1002/adma.200502053
4. Costa M, Klein CB (2006) Toxicity and carcinogenicity of chromium compounds in humans. Crit Rev Toxicol 36:63–155. https://doi.org/10.1080/10408440500534032
5. Guergova D, Stoyanova E, Stoychev D, Avramova I, Stefanov P (2015) Self-healing effect of ceria electrodeposited thin films on stainless steel in aggressive 0.5 mol/L NaCl aqueous solution. J. Rare Earths 33:1212–1227. https://doi.org/10.1016/S1002-0721(14)60548-2
6. Creus J, Brezault F, Rebere C, Gadouleau M (2006) Synthesis and characterisation of thin cerium oxide coatings elaborated by cathodic electrolytic deposition on steel substrate. Surf Coat Technol 200:4636–4645. https://doi.org/10.1016/j.surfcoat.2005.04.027
7. Sun J, Wang G (2014) Preparation and corrosion resistance of cerium conversion coatings on AZ91D magnesium alloy by a cathodic electrochemical treatment. Surf Coat Technol 254:42–48. https://doi.org/10.1016/j.surfcoat.2014.05.054
8. Dabala M, Armelao L, Buchberger A, Calliari I (2001) Cerium-based conversion layers on aluminum alloys. Appl Surf Sci 172:312–322. https://doi.org/10.1016/S0169-4332(00)00873-4
9. Montemor MF, Trabelsi W, Zheludevich M, Ferreira MGS (2006) Modification of bis-silane solutions with rare-earth cations for improved corrosion protection of galvanized steel substrates. Prog Org Coat 57:67–77. https://doi.org/10.1016/j.porgcoat.2006.06.009
10. Boudellioua H, Hamlaoui Y, Tifouti L, Pedraza F (2019) Effects of polyethylene glycol (PEG) on the corrosion inhibition of mild steel by cerium nitrate in chloride solution. Appl Surf Sci 473:449–460. https://doi.org/10.1016/j.apsusc.2018.12.164
11. Thomas S, Birbilis N, Venkatraman MS, Cole IS (2012) Corrosion of zinc as function of pH. Corrosion 60:1–9. https://doi.org/10.5006/1.3676630
12. Pedraza F, Mahadik SA, Bouchaud B (2015) Synthesis ofceria based superhydrophobic coating on Ni_2OCr substrate via cathodic electrodeposition. Phys Chem Chem Phys 17:31750–31757. https://doi.org/10.1039/C5CP04723D
13. Zhitomirsky I (2002) Cathodic electrodeposition of ceramic and organoceramic materials. Fundam Asp Adv Colloid Interface Sci 97:279–317. https://doi.org/10.1016/S0001-8686(01)00068-9
14. K. Brunelli, F. Bisaglia, J. Kovac, M. Dabalà, Effects of cathodic electrodeposition parameters of cerium oxide film on the corrosion resistance of the (2024) Al alloy. Mater Corros 60(2009):514–520. https://doi.org/10.1002/maco.200805096
15. Hamlaoui Y, Pedraza F, Remazeilles C, Cohendoz S, Rebere C, Tifouti L, Creus J (2009) Cathodic electrodeposition of cerium-based oxides on carbon steel fromconcentrated cerium nitrate solutions. Part I. Electrochemical and analytical characterisation.

Mater Chem Phys 113:650–657. https://doi.org/10.1016/j.matchemphys.2008.08.027
16. Wu L-K, Liu L, Li J, Hu J-M, Zhang J-Q, Cao C-N (2010) Electrodeposition of cerium (III)-modified bis-[triethoxysilypropyl] tetra-sulphide films on AA2024-T3 (aluminum alloy) for corrosion protection. Surf Coat Technol 204:3920–3926. https://doi.org/10.1016/j.surfcoat.2010.05.027
17. Trabelsi W, Cecilio P, Ferreira MGS, Montemor MF (2005) Electrochemical assessment of the self-healing properties of Ce-doped silane solutions for the pre-treatment of galvanised steel substrates. Prog Org Coat 54:276–284. https://doi.org/10.1016/j.porgcoat.2005.07.006
18. Cabral AM, Trabelsi W, Serra R, Montemor MF, Zheludkevich ML, Ferreira MGS (2006) The corrosion resistance of hot dip galvanised steel and AA2024-T3 pre-treated with bis-[triethoxysilylpropyl] tetrasulfide solutions doped with $Ce(NO_3)_3$. Corros Sci 48:3740–3758. https://doi.org/10.1016/j.corsci.2006.01.010
19. Montemor MF, Trabelsi W, Lamaka SV, Yasakau KA, Zheludkevich ML, Bastos AC, Ferreira MGS (2008) the synergetic combination of bis-silane and CeO_2-ZrO_2 nanoparticles on the electrochemical behaviour on galvanized steel in NaCl solution. Electrochim Acta 53:5913–5922. https://doi.org/10.1016/j.electacta.2008.03.069
20. Ferreira JM Jr, Rossi JL, Baker MA, Hinder SJ, Costa I (2014) Deposition and characterization of a new mixed organic/inorganic cerium containing coating for the corrosion protection of eletrogalvanized steel. Int J Electrochem Sci 9:1827–1839
21. Hamlaoui Y, Tifouti L, Remazeilles C, Pedraza F (2010) Cathodic electrodeposition of cerium based oxides on carbon steel from concentrated cerium nitrate. Part II: influence of electrodeposition parameters and of the addition of PEG. Mater Chem Phys 120:172–180. https://doi.org/10.1016/j.matchemphys.2009.10.042
22. Ferreira JM Jr, Souza KP, Queiroz FM, Costa I, Tomachuk CR (2016) Electrochemical and chemical characterization of electrodeposited zinc surface exposed to new surface treatments. Surf Coat Technol 294:36–46. https://doi.org/10.1016/j.surfcoat.2016.03.023
23. Kong G, Liu L, Lu J, Che C, Zhong Z (2011) Corrosion behavior of lanthanum-based conversion coating modified with citric acid on hot dip galvanized steel in aerated 1 M NaCl solution. Corros Sci 53:1621–1626. https://doi.org/10.1016/j.corsci.2011.01.038
24. Wang AQ, Golden TD (2003) Anodic electrodeposition of cerium oxide thin films I. Formation of crystalline thin films. J Electrochem Soc 150:C616–C620. https://doi.org/10.1149/1.1596164
25. Golden TD, Wang AQ (2003) Anodic electrodeposition of cerium oxide thin films II. Mechanism studies. J Electrochem Soc 150:C621–C624. https://doi.org/10.1149/1.1596165
26. Bourenane N, Pedraza F, Hamlaoui Y, Remazeilles C (2019) Effect of the pH of the electrolyte on the formation and on the corrosion properties of ceria based coating on carbon steel. Mater Corros 70:110–119. https://doi.org/10.1002/maco.201810302
27. Boudellioua H, Hamlaoui Y, Tifouti L, Pedraza F (2020) Effect of the temperature of cerium nitrate–NaCl solution on corrosion inhibition of mild steel. Mater Corros 71(8):1–10. https://doi.org/10.1002/maco.201911472
28. Zhitomirsky I, Petric A (2001) Electrochemical deposition of ceria and doped ceria films. Ceram Int 27:149–155. https://doi.org/10.1016/S0272-8842(00)00054-7
29. Zhou Y, Switzer JA (1996) Growth of cerium (IV) oxide films by the electrochemical generation of base method. J Alloys Compd 237:1–5. https://doi.org/10.1016/0925-8388(95)02048-9
30. Stefanov P, Atanasova G, Stoychev D, Marinova T (2004) Electrochemical deposition of CeO_2 on ZrO_2 and Al_2O_3 thin films formed on stainless steel. Surf Coat Technol 180–181:446–449. https://doi.org/10.1016/j.surfcoat.2003.10.083
31. Pour-Ghaz M, BurkanIsgor O, Ghods P (2009) The effect of temperature on the corrosion of steel in concrete. Part 1: simulated polarization resistance tests and model development. Corros Sci 51:415–425. https://doi.org/10.1016/j.corsci.2008.10.034
32. Sankara Narayanan TSN (2005) Surface pretreatment by phosphate conversion coatings—a review. Rev Adv Mater Sci 9:130–177
33. Jegannathan S, Sankara Narayanan TSN, Ravichandran K, Rajeswari S (2006) Formation of zinc–zinc phosphate composite coatings by cathodic electrochemical treatment. Surf Coat Technol 200:4117–4126. https://doi.org/10.1016/j.surfcoat.2005.04.022
34. Hamlaoui Y, Rémazeilles C, Bordes M, Tifouti L, Pedraza F (2010) Electrodeposition of ceria based layers on zinc electroplated steel. Corros Sci 52:1020–1025. https://doi.org/10.1016/j.corsci.2009.11.027
35. Hamlaoui Y, Pedraza F, Tifouti L (2008) Corrosion monitoring of galvanised coatings through electrochemical impedance spectroscopy. Corros Sci 50:1558–1566. https://doi.org/10.1016/j.corsci.2008.02.010
36. Wang AQ, Golden TD (2013) Electrodeposition of oriented cerium oxide films. Int J Electrochem. https://doi.org/10.1155/2013/482187
37. Chen H-I, Chang H-Y (2005) Synthesis and characterization of nanocrystalline cerium oxide powders by two-stage non-isothermal precipitation. Solid State Commun 133:593–598. https://doi.org/10.1016/j.ssc.2004.12.020
38. McConnell JS, McConnell RM, Hossner LR (1993) Ultraviolet spectra of acetic acid, glycine, and glyphosate. J Arkansas Acad Sci 47:73–76
39. Joshi S, Kulp EA, Fahrenholtz WG, O'Keefe MJ (2012) Dissolution of cerium from cerium-based conversion coatings on Al 7075-T6 in 0.1 M NaCl solutions. Corros Sci 60:290–295. https://doi.org/10.1016/j.corsci.2012.03.023
40. Chang HY, Chen HI (2005) Morphological evolution for CeO_2 nanoparticles synthesized by precipitation techniques. J Cryst Growth 283:457–468. https://doi.org/10.1016/j.jcrysgro.2005.06.002
41. Wen XG, Zhang WX, Yang SH (2002) Solution phase synthesis of $Cu(OH)_2$ nanoribbons by coordination self-assembly using cu_2s nanowires as precursors. Nano Lett 2:1397–1401. https://doi.org/10.1021/nl025848v
42. Montemor MF, Simoes AM, Ferreira MGS (2001) Composition and behaviour of cerium films on galvanised steel. Prog Org Coat 43:274–281. https://doi.org/10.1016/S0300-9440(01)00209-0
43. Kiyota S, Valdez B, Stoytchev M, Zlatev R, Bastidas JM (2011) Anticorrosion behavior of conversion coatings obtained from unbuffered cerium salts solutions on AA6061-T6. J Rare Earths 29:961–968. https://doi.org/10.1016/S1002-0721(10)60579-0
44. Wang Y-M, Zhao D-D, Zhao Y-Q, Xu C-L, Li H-L (2012) Effect of electrodeposition temperature on the electrochemical performance of a $Ni(OH)_2$ electrode. RSC Adv 2:1074–1082. https://doi.org/10.1039/C1RA00613D
45. Wang X, Fan F, Szpunar JA (2016) Optimizing cathodic electrodeposition parameters of ceria coating to enhance the oxidation resistance of a Cr_2O_3-forming alloy. Thin Solid Films 611:12–20. https://doi.org/10.1016/j.tsf.2016.05.004
46. Lu W, Huang P, Li K, Yan P, Wang Y, Yan B (2013) Effect of bath temperature on the microstructural properties of electrodeposited nanocrystalline FeCo films. Int J Electrochem Sci 8:2354–2364
47. Yang Y, Yang Y, Du X, Chen Y, Zhang Z (2014) Influences of the main anodic electroplating parameters on cerium oxide films. Appl Surf Sci 305:330–336. https://doi.org/10.1016/j.apsusc.2014.03.078
48. Lins SC, Reis GFA, Araujo CR, Matencio T (2006) Electrochemical impedance spectroscopy and linear polarization applied to evaluation of porosity of phosphate conversion coatings on

electrogalvanized steels. Appl Surf Sci 253:2875–2884. https://doi.org/10.1016/j.apsusc.2006.06.030
49. Su HY, Lins CS (2014) Effect of additives on the properties of phosphate conversion coating on electrogalvanized steel sheet. Corros Sci 83:137–146. https://doi.org/10.1016/j.corsci.2014.02.002
50. Abd-El-Nabey BA, El-Housseiny S, El-Kshlan HM (2017) Effect of surfactants on the protection efficiency of Zn-Phosphate coat on steel. Phys Chem 7:75–86. https://doi.org/10.5923/j.pc.20170704.01
51. Shainy KM, Ammal PR, Unni KN, Benjamin S, Joseph A (2016) Surface interaction and corrosion inhibition of mild steel in hydrochloric acid using pyoverdine, an eco-friendly bio-molecule. J Bio Tribo Corros 2:2–12. https://doi.org/10.1007/s40735-016-0050-3
52. Ferreira MGS, Duarte RG, Montemor MF, Simõs AMP (2004) Silanes and rare earth salts as chromate replacers for pre-treatments on galvanised steel. Electrochim Acta 49:2927–2935. https://doi.org/10.1016/j.electacta.2004.01.051
53. Deslouis C, Duprat M, Tournillon C (1989) The kinetics of zinc dissolution in aerated sodium sulphate solutions, a measurement of the corrosion rate by impedance techniques. Corr Sci 29:13–30. https://doi.org/10.1016/0010-938X(89)90077-2
54. Cachet C, Ganne F, Maurin G, Petitjean J, Vivier V, Wiart R (2001) EIS investigation of zinc dissolution in aerated sulfate medium. Part I: bulk zinc. Electrochim Acta 47:509–518. https://doi.org/10.1016/S0013-4686(01)00740-X
55. Le Manchet S, Landoulsi J, Richard C, Verchère D (2010) Study of a chromium-free treatment on hot-dip galvanized steel: electrochemical behaviour and performance in a saline medium. Surf Coat Technol 205:475–482. https://doi.org/10.1016/j.surfcoat.2010.07.009
56. Zhang X, van den Bos C, Sloof WG, Hovestad A, Terryn H, de Wit JHW (2005) Comparison of the morphology and corrosion performance of Cr(VI) and Cr(III)-based conversion coatings on zinc. Surf Coat Technol 199:92–104. https://doi.org/10.1016/j.surfcoat.2004.12.002
57. Cao CN, Zhang JQ (2002) An introduction to electrochemical impedance. Science Press, Beijing
58. Arurault L, Monsang P, Salley J, Bes RS (2004) Electrochemical preparation of adherent ceria coatings on ferritic stainless steel. Thin Solid Films 466:75–80. https://doi.org/10.1016/j.tsf.2004.02.039

Affiliations

F. Rouabhia[1] · Y. Hamlaoui[1] · A. Meroufel[2] · F. Pedraza[3]

✉ Y. Hamlaoui
hamlaoui_youcef@yahoo.fr

[1] Laboratoire de Physique de La Matière et Rayonnement (LPMR), Faculté des Sciences et de Technologie, Université Mohamed Chérif Messaadia, BP 1553, 41000 Souk-Ahras, Algeria

[2] RISE Kimab, 16440 Kista, Sweden

[3] Laboratoire des Sciences de L'Ingénieur Pour l'Environnement (LaSIE), UMR 7356 CNRS Pôle Science et Technologie, Université de la Rochelle, Avenue Michel Crepeau, 17042 La Rochelle Cedex 1, France